Journal of Solid State Chemistry **148,** 158–168 (1999)
Article ID jssc.1999.8441, available online at http://www.idealibrary.com on IDEAL®

Ordering of Oxygen Vacancies and Magnetic Properties in $La_{0.5}Ca_{0.5}MnO_{3-\delta}$ ($0 \leq \delta \leq 0.5$)

J. M. González-Calbet,*,†,[1] E. Herrero,*,† N. Rangavittal,‡ J. M. Alonso,†,§ J. L. Martínez,§ and M. Vallet-Regí†,‡

*Departamento de Química Inorgánica, Facultad de Químicas, Universidad Complutense, 28040 Madrid, Spain; †Instituto de Magnetismo Aplicado, RENFE-UCM, Apdo. 155, 28230 Las Rozas, Spain; ‡Departamento de Química Inorgánica y Bioinorgánica, Facultad de Farmacia, Universidad Complutense, 28040 Madrid, Spain; and §Instituto de Ciencia de Materiales de Madrid, CSIC, Cantoblanco, 28049 Madrid, Spain

Received December 31, 1998; in revised form June 15, 1999; accepted July 2, 1999

IN HONOR OF PROF. C. N. R. RAO ON HIS 65TH BIRTHDAY

The study by electron diffraction and high resolution electron microscopy of several samples of the system $La_{0.5}Ca_{0.5}MnO_{3-\delta}$, apart from strikingly confirming the correctness of the orthorhombic perovskite-related unit cell of $a \approx a_c\sqrt{2}$, $b \approx a_c\sqrt{2}$, $c \approx 2a_c$ for $0 \leq \delta \leq 0.25$, points to the existence of three dimensional multitwinning which gives rise to an apparently double cubic cell. For $\delta = 0.5$, the ordering of the anionic vacancies leads to a new material isostructural to Sr_2FeO_5 and unit cell $a = 5.361(3)$, $b = 16.463(9)$, $c = 5.340(3)$ Å, space group *Ibm*2. The magnetic characterization of the three compositions has been carried out and related to the structure. © 1999 Academic Press

Key Words: **colossal magnetoresistance; $La_{0.5}Ca_{0.5}MnO_{3-\delta}$; twinning in perovskites.**

INTRODUCTION

Perovskite-related manganese oxides have been intensively studied for the past several years in order to understand the colossal magnetoresistance (CMR) exhibited by this system. A significant contribution in the compositional and structural changes in the $RE_{1-x}M_xMnO_3$ system (RE = La, Nd, Gd, Y; M = Ca, Sr, Ba, Pb) and their effects in either magnetic properties, such as the magnitude of magnetoresistance and the ferromagnetic transition temperature, or in the electron transport properties, in particular charge-ordering effects, has been made by Rao and his group (1–19).

CMR was reported for the $La_{1-x}M_xMnO_3$ (M = Ca, Sr, Ba) system in bulk and in thin films (20–22), the occurrence of giant magnetoresistance being linked to the presence of an optimal proportion of Mn^{4+} ions (5). In the case of the undoped material $LaMnO_{3+\delta}$ ($\delta = 0$), the Mn ions are formally trivalent with the electronic configuration of $t_{2g}^3e_g^1$. Lattice defects such as cation vacancies and/or substitution of divalent cations for La^{3+} can dope holes into the e_g levels resulting in a formally mixed valence Mn^{3+}/Mn^{4+} matrix where these doped holes may be localized or itinerant. The different types of magnetic ordering present in the system $La_{1-x}M_xMnO_{3+\delta}$ (M = Ca, Sr) depend on the value of x. The Mn^{3+}–O–Mn^{4+} exchange interaction is ferromagnetic due to the fact that the e_g itinerant electron is exchanged between Mn^{3+} and Mn^{4+} ions by the so-called double exchange mechanism (23) while the Mn^{3+}–O–Mn^{3+} and Mn^{4+}–O–Mn^{4+} superexchange interactions are antiferromagnetic. The complete phase diagram of $La_{1-x}Ca_xMnO_3$ was obtained for the first time through magnetization and resistivity measurements over a broad range of temperatures and concentrations (24). Near $x = 0.5$, the ground state changes from a ferromagnetic conductor to an antiferromagnetic insulator, which according to several authors (19, 25, 26) is associated to a charge ordering state. The phase diagram of several related perovskite-type manganites with fixed doping levels of $x = 0.5$, $RE_{0.5}Sr_{0.5}MnO_3$ (RE = Nd, Sm, Pr, La) reported by Tokura *et al.* (27, 28) reveals that the competition between the ferromagnetic double-exchange and antiferromagnetic charge-ordering instability gives rise to a lattice-coupled first-order phase transition induced by a relatively low magnetic field.

The introduction of anionic vacancies must necessarily affect both the magnetic and transport properties. Many models have been proposed to explain the vacancy distribution in the undoped $LaMnO_3$ systems. The first and foremost model proposed by Tofield and Scott (29) explains the oxygen excess in the form of La as well as Mn vacancies in the structure, with the greater proportions of the former.

[1]To whom correspondence should be addressed at: Departamento de Química Inorgánica, Facultad de Químicas, Universidad Complutense, 28040 Madrid, Spain. Fax: 34 91 394 43 52; E-mail: jgcalbet@eucemax.sim.ucm.es.

0022-4596/99 $30.00
Copyright © 1999 by Academic Press
All rights of reproduction in any form reserved.

Kuo *et al.* (30) have proposed that the vacancies in the A and B sites are likely to be in equal amounts and with the possibility of La vacancies present along with the oxygen vacancies. Van Roosmalen and co-workers (31, 32) have demonstrated from neutron powder diffraction and density measurements that oxygen excess cannot be accommodated in $LaMnO_{3+\delta}$ where Mn^{4+} is created by the presence of random distribution of La and Mn vacancies in equal amounts but with the oxygen sublattice fully occupied. The presence of substantially higher proportions of Mn vacancies depending sensitively on the oxidation conditions has been also reported (33). Similar considerations also apply for the Ca and Sr doped $La_{1-x}M_xMnO_3$ materials.

On the other hand, it is well known that some Mn perovskites are catalysts which readily release oxygen from the selective oxidation of hydrocarbons, in the process forming nonstoichiometric phases up to $\delta = 0.5$ as in $CaMnO_{3-\delta}$ (34). The three dimensionally linked MnO_6 octahedra present in $CaMnO_3$ on reduction convert to MnO_5 square pyramids and on proceeding from $CaMnO_3$ to $CaMnO_{2.5}$ (35) the proportions of the MnO_5 square pyramids increases and the MnO_6 octahedra decreases. In total five distinct compositions grossly nonstoichiometric consisting of superstructures formed by the ordering of vacancies have been reported (36). Thus the $La_{1-x}Ca_xMnO_{3+\delta}$ perovskite system should also undergo similar selective redox reactions to render oxygen deficient phases under reducing atmosphere.

In the view of the fascinating magnetic and electrical properties of the $LaMnO_3$, its substituted derivatives, and its ability to lose and take oxygen we consider it interesting to study the $La_{0.5}Ca_{0.5}MnO_{3-\delta}$ ($0 \le \delta \le 0.5$) system containing varying percentages of Mn^{4+}, to understand the type of vacancy ordering by using selected area electron diffraction (SAED) and high resolution electron microscopy (HREM) and its influence on the magnetic properties.

EXPERIMENTAL

The oxidized sample of $La_{0.5}Ca_{0.5}MnO_3$ was prepared by ceramic method by heating in air stoichiometric amounts of the corresponding oxides or carbonates at 1400°C for 110 h. Samples with anionic vacancies were obtained by controlled reduction under H_2/He of the samples prepared in air. Chemical analysis was performed to obtain the nominal atomic ratio using an atomic absorption technique. Thermogravimetric measurements performed on a CAHN D-200 electrobalance indicate that the oxygen stoichiometry per unit formula is 3.0 with an equal percentage of Mn^{3+} and Mn^{4+}. The reduction of the $La_{0.5}Ca_{0.5}MnO_3$ sample was carried out in the CAHN D-200 electrobalance. The formation of $La_{0.5}Ca_{0.5}MnO_{3-\delta}$ ($\delta = 0.25,\ 0.5$) by the reduction of $La_{0.5}Ca_{0.5}MnO_3$ on loosing 0.25 and 0.5 oxygen, respectively, per unit formula is shown in the thermogravimetric plot in Fig. 1. The samples of both oxidized and reduced ones were characterized by powder X-ray diffraction. Figures 2 (a–c) shows the indexed X-ray diffraction patterns of the $La_{0.5}Ca_{0.5}MnO_{3-\delta}$ ($\delta = 0.0,\ 0.25,\ 0.5$) samples, respectively. SAED and HREM were performed by using both JEOL 2000 FX and JEOL 4000 EX electron microscopes. Samples were ultrasonically dispersed in *n*-butanol and then mounted on carbon-coated microgrids.

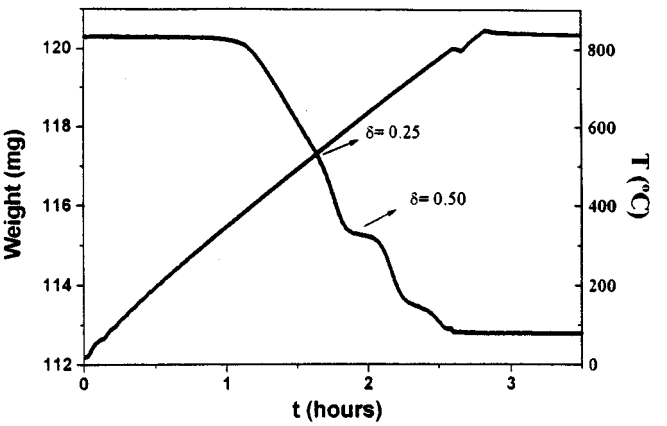

FIG. 1. Thermogravimetric curve of $La_{0.5}Ca_{0.5}MnO_{3-\delta}$ showing the oxygen loss corresponding to the formation of $\delta = 0.25$ and 0.5 compositions.

The magnetic properties were obtained in a SQUID magnetometer in the temperature range from 5 to 400 K. The transport characterization was made by the DC constant current with standard four-terminals technique under magnetic fields up to 9 T.

RESULTS AND DISCUSSION

The structure of the $La_{1-x}A_xMnO_3$ (A = Ca, Sr) system is complex due to the structural distortions which lead to a variety of closely related pseudo-cubic crystal structures. These distortions depend on the cation and oxygen stoichiometry as well as synthesis conditions and are typical of the cubic packed pervoskites (37, 38). The predominant structures are cubic (*Pm3m*, $a \approx a_p$, $Z = 1$, or *Fm3m*, $a \approx 2a_p$, $Z = 8$), the $GdFeO_3$-type orthorhombic (*Pbnm*, $a \approx b \approx \sqrt{2}a_p$, $c = 2a_p$, $Z = 4$) or $LaAlO_3$-type rhombohedral/hexagonal ($R\bar{3}c$, $a \approx \sqrt{2}a_p$, $\alpha \approx 60.5°$, $Z = 2$ or $a \approx 2a_p$, $c \approx 2\sqrt{3}a_p$, $Z = 6$) (5, 39, 40) and there are reports of monoclinic ($P2_1/c$) and another orthorhombic structure (*Imma*, at low temperature) (41, 42). All these structures are closely related and therefore have similar free energy of formation. In this study, the X-ray diffraction pattern of the compound $La_{0.5}Ca_{0.5}MnO_3$ is indexed in the space group *Pbnm*.

However, the SAED study shows a more complex situation. Figure 3a shows the SAED pattern along the $[001]_c$

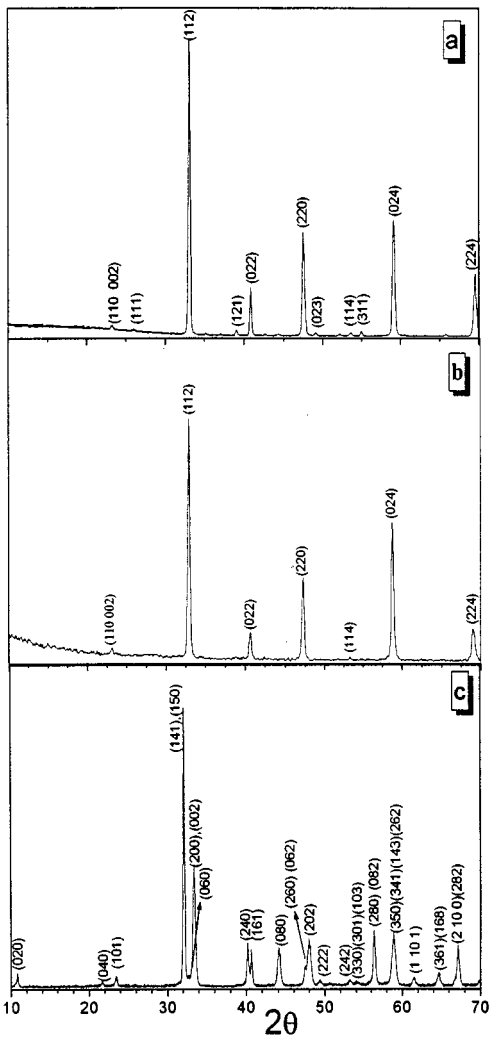

FIG. 2. X-ray powder diffraction patterns of $La_{0.5}Ca_{0.5}MnO_{3-\delta}$. (a) $\delta = 0$ (b) $= 0.25$, (c) $\delta = 0.5$.

axis,[2] which could be indexed on the basis of a double perovskite cell. Figure 3b shows the SAED pattern corresponding to another area of the same crystal. It can be observed that some spots have disappeared. The corresponding HREM image (Fig. 3c) indicates that the situation corresponds actually to a multitwinning involving two individual orthorhombic domains. In each of the individual domains the double perovskite axis was at random in one of the three space directions. The regions marked B and C correspond to each domain, and the corresponding diffraction patterns of each domain are schematically shown in Fig. 3b. It is clear that the selected area diagram covering the regions of contact of the two types of the domains will give an electron diffraction pattern similar to that of Fig. 3b.

[2]Subindex c refers to the cubic perovskite subcell.

It is worth pointing out that a slight distortion of $\approx\sqrt{2}a_c \times \approx\sqrt{2}a_c \times 2a_c$ is not obvious in the powder X-ray diffraction pattern or in the electron diffraction pattern since the orthorhombic distortion is extremely small that favors the formation of the three dimensional twinning. Such a type of multitwinning has been reported in several slightly distorted orthorhombic perovskite-related systems (43–45).

The sample $La_{0.5}Ca_{0.5}MnO_3$ on reduction loses oxygen gradually and two different oxygen deficient phases such as $La_{0.5}Ca_{0.5}MnO_{2.75}$ and $La_{0.5}Ca_{0.5}MnO_{2.5}$ could be stabilized. The X-ray diffraction pattern of the compound $La_{0.5}Ca_{0.5}MnO_{2.75}$ shown in Fig. 2b is similar to that of $La_{0.5}Ca_{0.5}MnO_3$ and could be indexed in the orthorhombic system with the space group *Pbnm*. The electron diffraction pattern of this compound is shown in Fig. 4a. As in the previous case, the SAED pattern of this phase at first sight seems to be that of a two-fold superstructure of the basic perovskite. But once again the corresponding high resolution image (Fig. 4b) reveals a multitwinned situation as seen in $La_{0.5}Ca_{0.5}MnO_3$. The area represented in the micrograph shows that three individual domains coexist. Regions marked A, B, C correspond to the individual domains and the corresponding electron diffraction patterns are schematically shown below the SAED patterns of each domain. It is obvious from the high resolution image that the SAED pattern taken covers the three types of domains which can be interpreted as the juxtaposition of the three SAED patterns from the regions A, B, C. However, the difference between the structure of $La_{0.5}Ca_{0.5}MnO_3$ and $La_{0.5}Ca_{0.5}MnO_{2.75}$ is that the size of the microdomains is much smaller in the latter compound. This suggests that the domain size decreases as the concentration of the anionic vacancies increases showing that to a certain extent the defects are accommodated in the form of microdomains since oxygen vacancies seem to be accommodated in the domain walls.

The microdomain walls as seen here can be rationalized by considering them as intermixtures in three dimensions of a few high-index interface surfaces which, because of their inherent pseudosymmetry, possess sets of coincident sites that are suitable for the formation of low-energy compositional planes. This kind of environment is established purely by the partial distortion of the regular octahedral framework where the octahedra can be considered as a structural block which remains invariant as they undergo topological distortion. Such a concept was proposed by White *et al.* (43) in a study of twin boundaries in the $CaTiO_3$ perovskite system using Glazer's notation of octahedral tilt (46). The transition metal (in this case Mn) atoms retain their centrosymmetric position all through the lattice and the oxygen arrays undergo additional distortion at the compositional plane. If the parent O and Ca (in this case La and Ca) arrays are superimposed, the maximum mismatch of the coincident

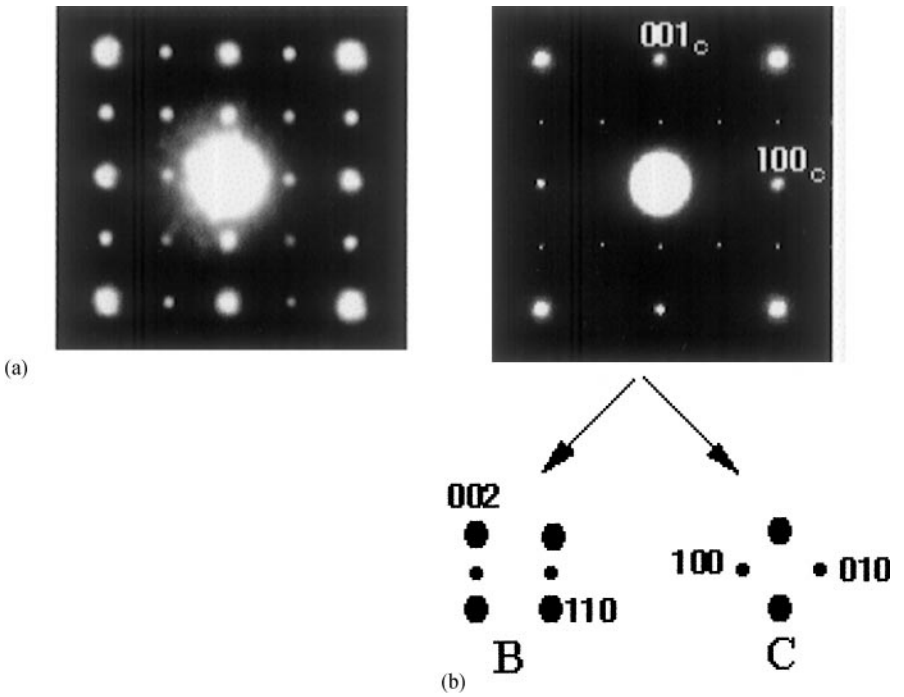

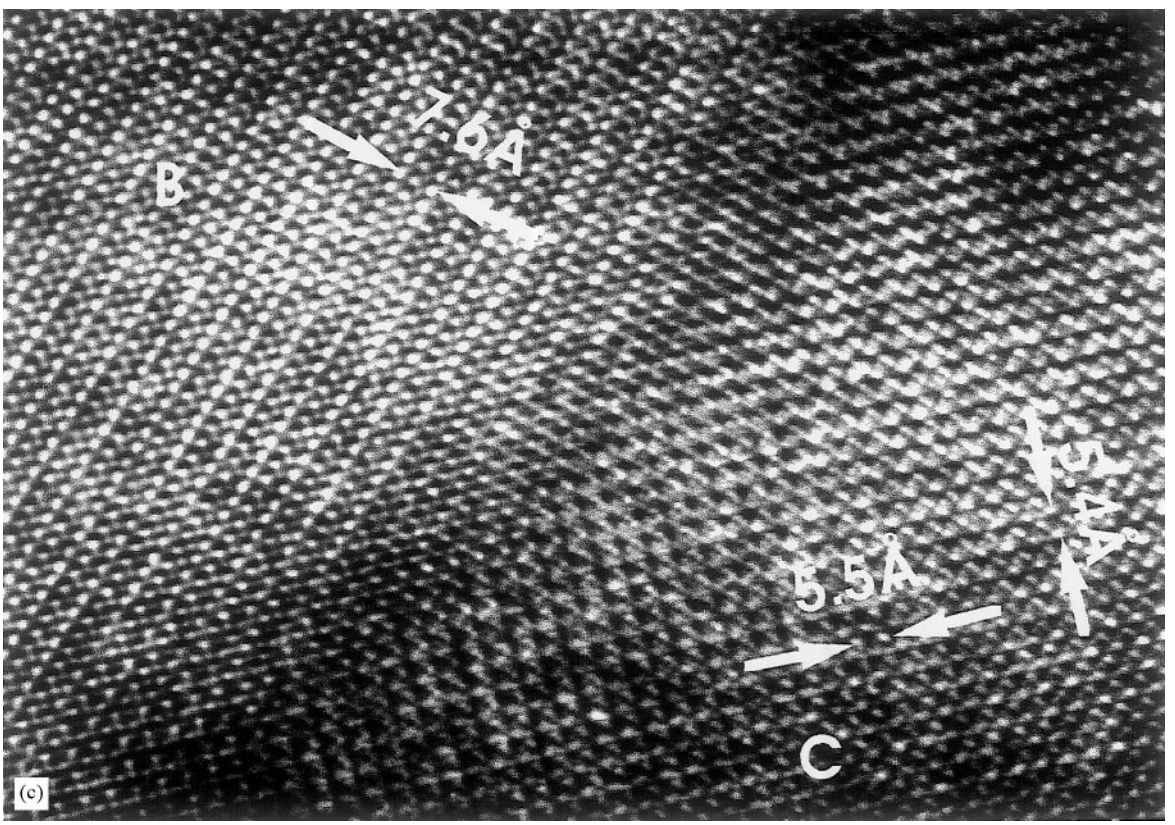

FIG. 3. (a) SAED pattern corresponding to $La_{0.5}Ca_{0.5}MnO_3$ along the $[001]_c$ axis. (b) SAED pattern corresponding to another area of the same crystal. (c) HREM image involving two individual domains represented by B and C. The schematic representation corresponding to the electron diffraction patterns of each domain $[1\bar{1}0]$ and [001] is shown in (b).

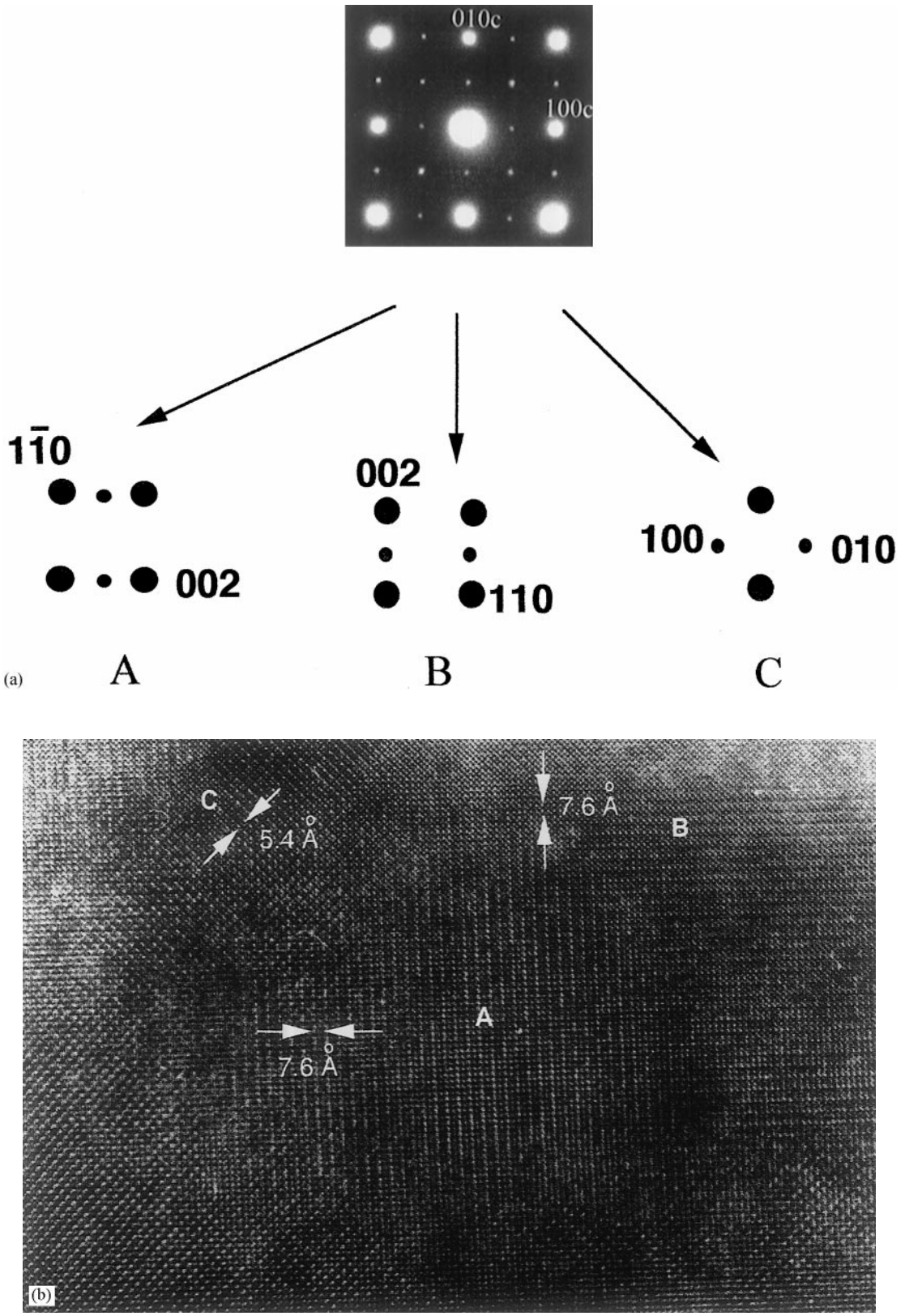

FIG. 4. (a) SAED pattern corresponding to $La_{0.5}Ca_{0.5}MnO_{2.75}$ along $[001]_c$. (b) Corresponding high resolution image showing microdomains involving juxtapositioning of three individual domains represented by A, B, and C. The electron diffraction patterns of the individual domains are schematized below the SAED pattern.

sites is much less compared to the mismatch seen in the compositional planes. Since the Mn atoms are not displaced from their special positions it is anticipated that the transition metal (Mn) array will suffer minimal distortion and should be almost perfectly coherent across the interface. Thus, when the parent perovskite is subjected to topotactic reduction, the transition metal undergoes a change in the oxidation state leading to the distortion in the oxygen network and formation of compositional planes. For simple examples such as perovskites, where in the compositional planes they are well defined and planar, it is possible to consider the formation of such boundaries as a way of generating thin, lamellar intergrowths of other perovskite polytypes within the parent structure. Such twin boundaries could propagate through a real crystal without destroying the integrity of the octahedral network and it is common to see more of such boundaries leading to the formation of more composition planes on further reduction. The anion-deficient phase tends to form differently oriented microdomains up to a certain extent of oxygen deficiency. A possible explanation for the different orientations of these domains lies in the unequal distortion of the octahedra within the perovskite structure.

The sample $La_{0.5}Ca_{0.5}MnO_{2.75}$ on further reduction converts to $La_{0.5}Ca_{0.5}MnO_{2.5}$. The X-ray diffraction pattern of this phase is shown in Fig. 2c. The cell parameters of this phase obtained from the X-ray diffraction analysis are $a = 5.361(3)$ Å. $b = 16.436(9)$ Å, $c = 5.340(3)$ Å, which is consistent with the values obtained from SAED patterns. The SAED patterns corresponding to the [100] and [10$\bar{1}$] zone axes are shown in Figs. 5a and 5b. Rietveld profile refinement of the X-ray powder diffraction was done with the model of $Sr_2Fe_2O_5$ structure crystallizing in the *Ibm*2 space group consisting of octahedra and oppositely oriented tetrahedral units (47). The profile refinement done with the coordinates of $Sr_2Fe_2O_5$ (47) resulted in a satisfactory agreement with the calculated and experimental (*hkl*), with a $R_p = 12.01$, $R_{w.p} = 16.06$, $R_{I,hkl} = 11.56$, though with a higher $R_{w.p}$. As a further test, the SAED patterns were simulated with the coordinates of the $Sr_2Fe_2O_5$ type for the [100] and [101] zone axes, giving a good agreement with the experimental SAED patterns, as shown in Figs 5a and

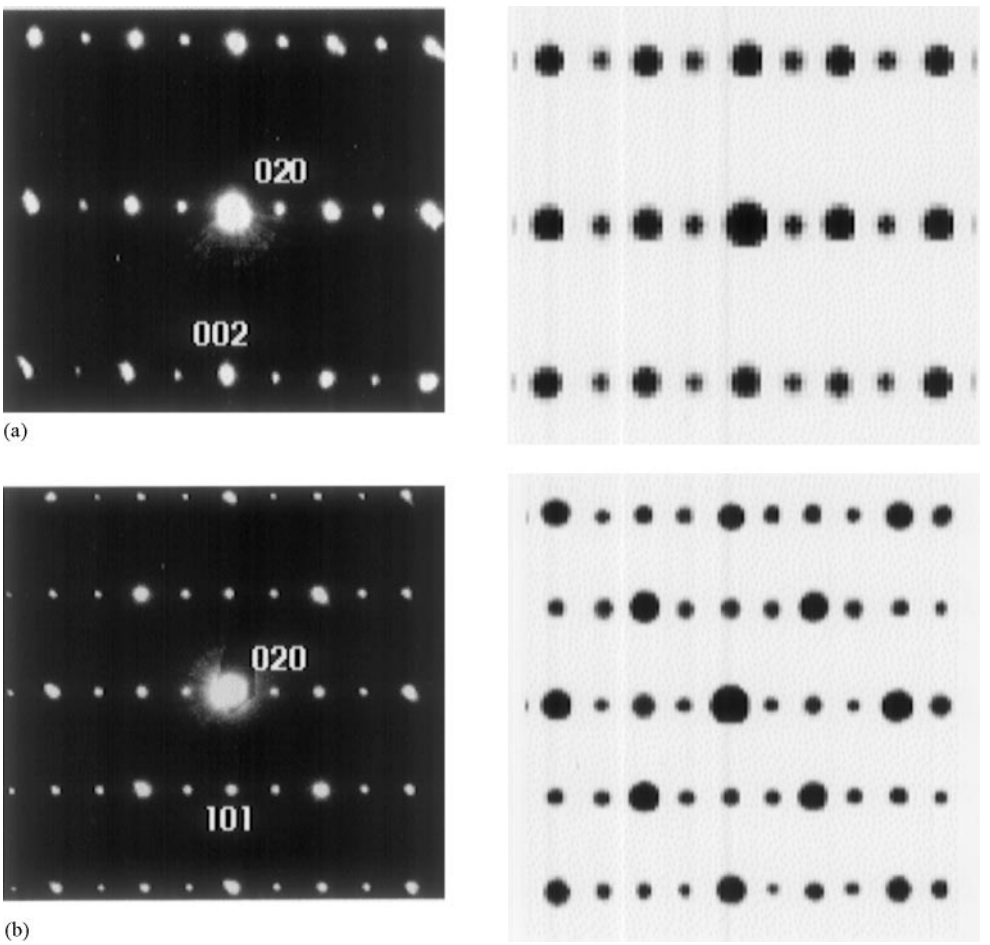

FIG. 5. Experimental and simulated SAED patterns corresponding to $La_{0.5}Ca_{0.5}MnO_{2.5}$ along (a) [100] and (b) [10$\bar{1}$] zone axes.

5b. Two structural projections were drawn using the coordinates of the $Sr_2Fe_2O_5$-type model. One along the [100] orientation and the other one tilting this to [10$\bar{1}$], as shown in Figs. 6a and 6b, suggesting that the structure is similar to that of $Sr_2Fe_2O_5$ with alternate [MnO_6] octahedra and [MnO_4] tetrahedral like coordination. The structure of $Sr_2Fe_2O_5$ is different from that of the brownmillerite-type $Ca_2Fe_2O_5$, though both these structures are derived by the reduction of ABO_3 perovskite-type structure with the oxygen vacancies ordered along alternate rows (48). In this way, half-octahedral sites are transformed into tetrahedral sites. The significant difference between both these structures is with respect to the orientation of the tetrahedral unit and more particularly in the position of the tetrahedrally surrounded Fe atom and one of the oxygen atoms sharing the corners of the tetrahedra. However, the system $LaSrCuAlO_5$ which is related to the brownmillerite-type structure crystallizes with a unit cell dimension of $a = 2a_c$, $b = 2a_c\sqrt{2}$, $c = \sqrt{2}a_c$, with Cu in octahedral and Al in tetrahedral coordination, leading to rows of vacancies aligned in every Al tetrahedral layer (49). It is known that $CaMnO_3$ on reduction to $CaMnO_{2.5}$ results in a structure consisting of oppositely oriented [MnO_5] square pyramids. $CaMnO_{2.5}$ crystallizes with the cell dimension $a = 5.424$ Å, $b = 10.230$ Å, $c = 3.735$ Å in the space group *Pbam* (35). In this $Sr_2Fe_2O_5$-type structure, the loss of 0.5 oxygens per unit formula results in a structure consisting of [MnO_6] octahedra and a removal of

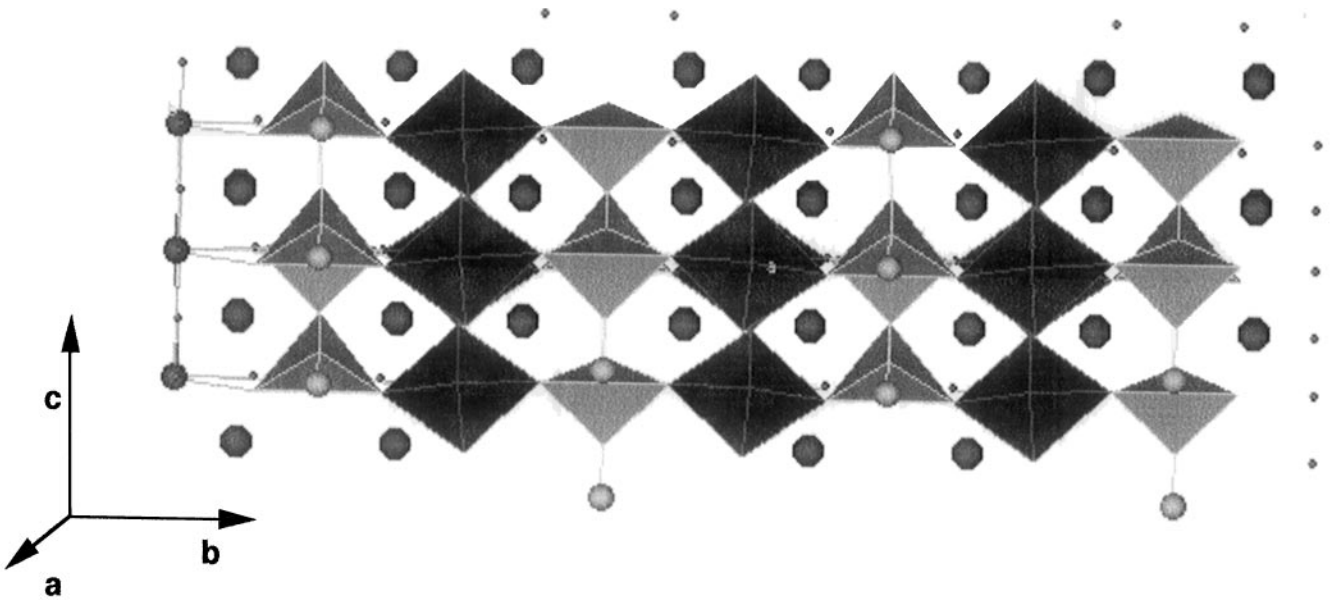

(a)

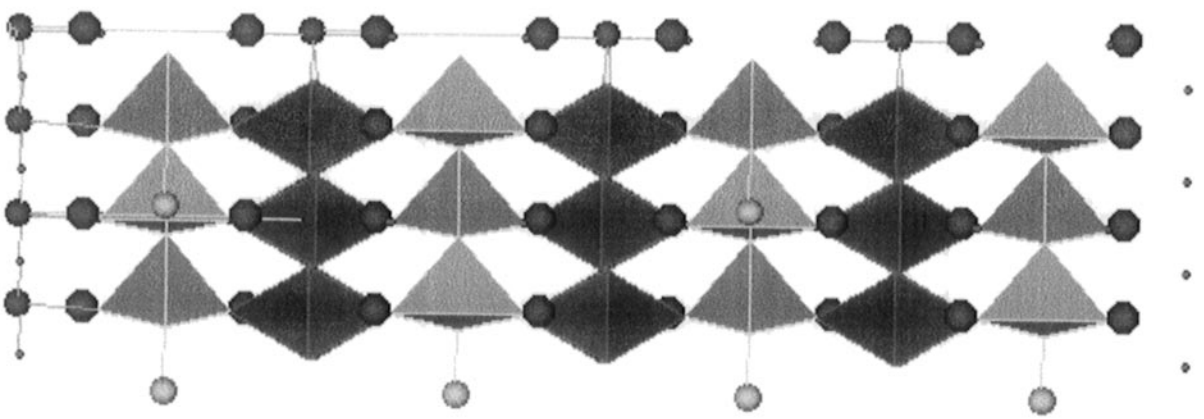

(b)

FIG. 6. Structural projections of $La_{0.5}Ca_{0.5}MnO_{2.5}$ along (a) [100] and (b) [10$\bar{1}$] orientation.

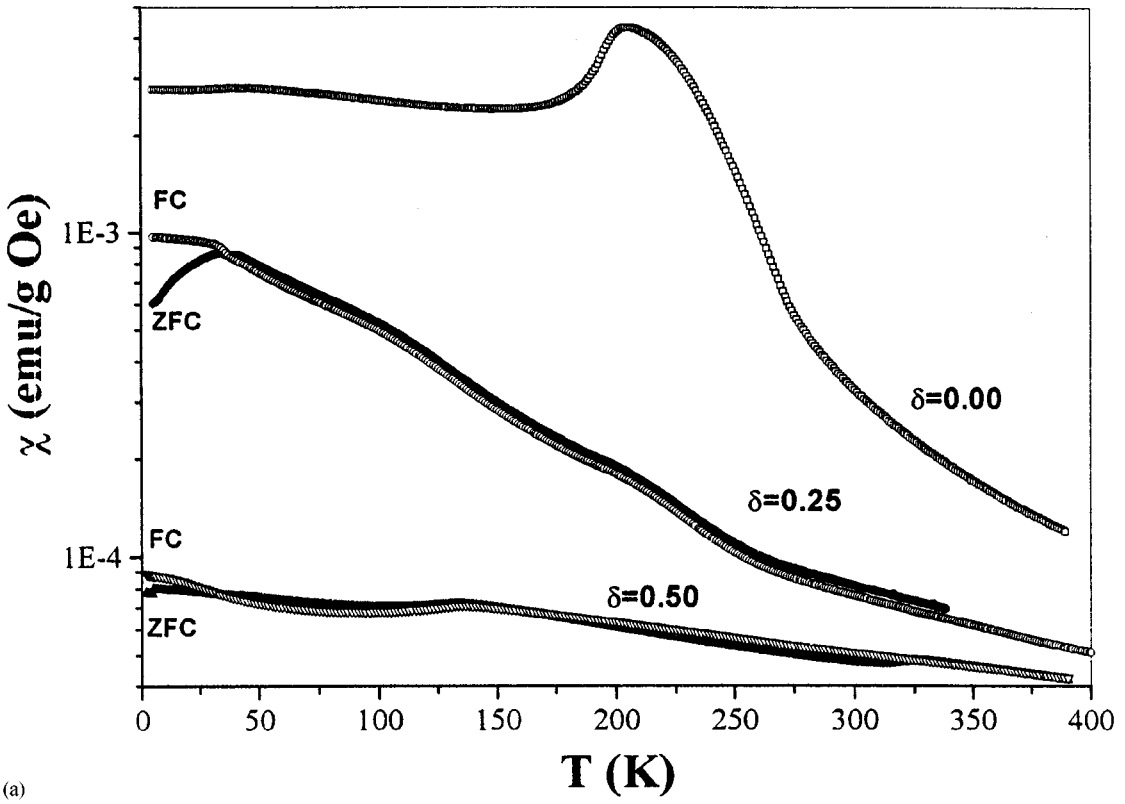

(a)

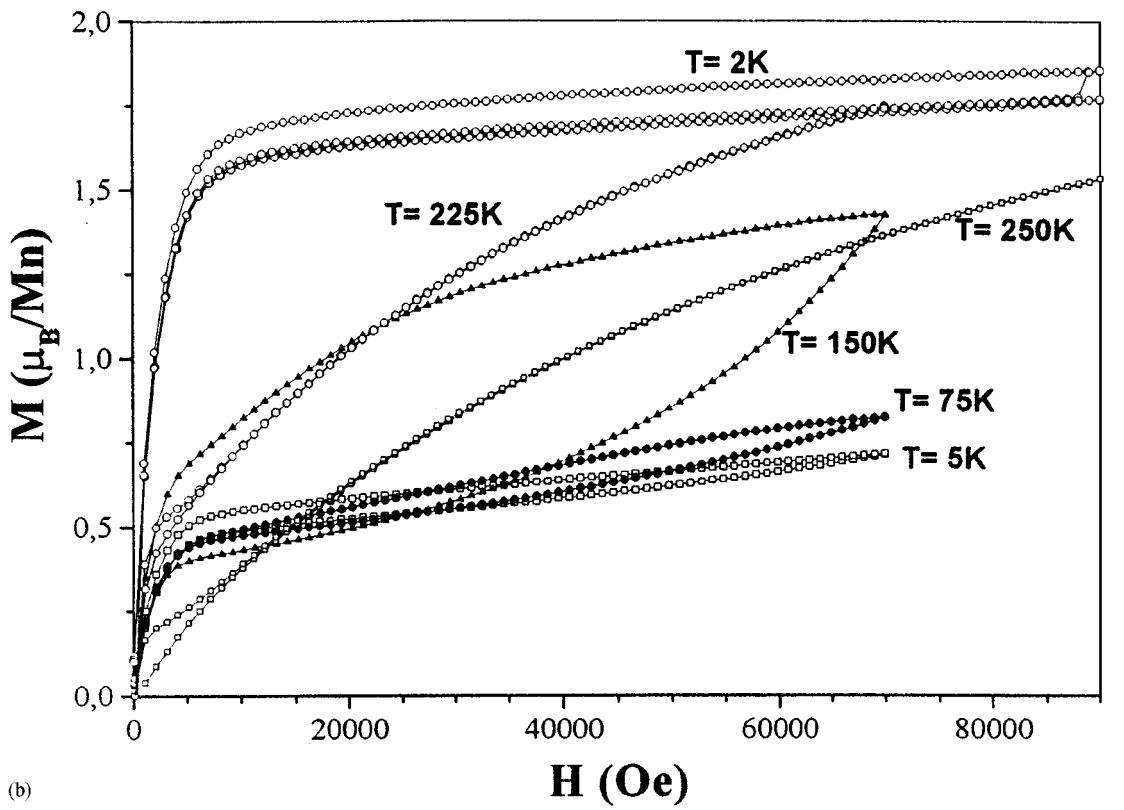

(b)

FIG. 7. (a) Temperature dependence of magnetic susceptibility χ(T) measured at 1 kOe field for $La_{0.5}Ca_{0.5}MnO_{3-\delta}$ ($\delta = 0.0, 0.25, 0.5$). (b) Hysteresis loops for $La_{0.5}Ca_{0.5}MnO_{3.00}$.

oxygen from the in-plane site leading to a tetrahedral-like coordination.

The charge balance in $La_{0.5}Ca_{0.5}MnO_{2.5}$ suggests that the average oxidation state of Mn is 2.5, which would fit to 50% of Mn^{3+} and 50% of Mn^{2+}, with Mn^{3+} in tetrahedral coordination and Mn^{2+} in octahedral coordination due to its ionic radii. However, there are no reports showing the presence of Mn^{3+} in tetrahedral coordination. In fact, in the table of the effective ionic radii of Shannon (50), Mn^{3+} is shown to be present only in V and VI coordination. If, according to that, Mn^{3+} cannot be in tetrahedral coordination, all Mn^{3+} should be present in octahedral and all Mn^{2+} in tetrahedral coordination. Assuming this fact and taking into account the ionic radii of Shannon ($^{IV}r_{Mn^{2+}} = 0.66$ Å, and $^{VI}r_{Mn^{3+}} = 0.83$ Å), the estimate of the c parameter of 16.02 Å is quite far from the experimental value of 16.436 Å.

Van Roosmalen *et al.* (31, 32, 51, 52) have stated that the oxygen excess in $LaMnO_{3+\delta}$ is incorporated by the partial charge disproportionation of Mn^{3+} into Mn^{2+} and Mn^{4+}. Considering the possibility of charge disproportionation of Mn^{3+}, the oxidation state of the manganese in $La_{0.5}Ca_{0.5}MnO_{2.5}$ would lead to 25% of Mn^{4+} and 75% of Mn^{2+}, both of which could occupy the IV and VI coordination. In such a case, there exist two possibilities, the first one wherein the Mn^{4+} is in tetrahedral coordination ($^{VI}r_{Mn^{4+}} = 0.39$ Å) (since Mn^{4+} has a lower ionic radii than Mn^{2+}) for which case the c parameter calculated is 16.22 Å.

However, a disproportionation mechanism is less justified in a reduction process as compared to the incorporation of oxygen in $LaMnO_{3+\delta}$. In this case, it is worth recalling that $La_{0.5}Ca_{0.5}MnO_{2.50}$ has been obtained by reduction of $La_{0.5}Ca_{0.5}MnO_3$ where both Mn^{3+} and Mn^{4+} are octahedrally coordinated. A possible reduction mechanism to give 75% Mn^{2+} and 25% Mn^{4+} would assume the initial reduction of Mn^{3+} to Mn^{2+} and the change of Mn^{4+} to Mn^{2+}. In fact, in the thermogravimetric measurement, two different kinetics are observed since a change in the slope is apparent at $\delta = 2.75$ (Fig. 1). If this is true, it seems logical that Mn^{4+} would stay in octahedral coordination and Mn^{2+} would stay in both octahedral and tetrahedral coordination leading again to a calculated c parameter equal to 16.20 Å. Moreover, an argument supporting this reduction mechanism is that such a reduction should lead to an intermediate stage in which 50% Mn^{4+} and 50% Mn^{2+} coexist leading to $La_{0.5}Ca_{0.5}MnO_{2.75}$, while a disproportionation mechanism should imply a reduction in only one step leading to $La_{0.5}Ca_{0.5}MnO_{2.50}$.

Figure 7a shows the temperature dependence of magnetic susceptibility $\chi(T)$ measured in a 1 kOe field for the $La_{0.5}Ca_{0.5}MnO_{3-\delta}$ samples ($\delta = 0.0$, 0.25, 0.50). For $\delta = 0.0$, the susceptibility behavior as reported (53) presents three clear anomalies. The first one corresponds to a transition from paramagnetic to an almost ferromagnetic state at $T_c \approx 254$ K. At lower temperature, there is a clear drop in the susceptibility ($T_{CO} \approx 190$ K), probably due to the charge ordering (localization) of the charge carriers. Later, at lower temperature, a cusp is observed in the magnetic susceptibility close to the temperature value which for different reduced samples ($\delta = 0.25$), strong differences for field and zero field cooling processes are observed. The paramagnetic moment for this system is 5.02 μ_B per formula, which is rather higher than the expected value of 4.35 μ_B per formula, corresponding to an average Mn oxidation state of 3.5 (50% Mn^{4+}, 50% Mn^{3+}) (see Table 1).

This view is oversimplified due to the fact that for this concentration probably different magnetic phases coexist and the first order transition of the charge ordering state presents very strong hysteretic behavior (Fig. 7b). It is interesting to point out that at 2 K, a clear ferromagnetic (or superparamagnetic) behavior is observed with a saturation moment of 1.8 μ_B/Mn. Nevertheless, the saturation value in the ordered state is always below the expected, i.e., $\mu_B = 1.0$ μ_B/Mn at 225 K and $\mu_s = 0.5$ μ_B/Mn at 5 K.

The creation of anionic vacancies produces a big drop in the magnetic susceptibility. For $\delta = 0.25$, there is some reminiscence of the charge ordering at $T \approx 200$ K and a clear irreversibility at 40 K, which could indicate a glassy behavior at low temperature, probably induced by the lack of oxygen in the superexchange interaction path. For $\delta = 0.50$, the susceptibility is much lower, with an irreversibility at $T \approx 30$ K.

Also the transport measurements of this system are very sensitive to the creation of anionic vacancies. The temperature dependence of the resistivity for two magnetic fields (0 and 9 T), corresponding to $La_{0.50}Ca_{0.50}MnO_{3.00}$, is shown in Fig. 8a. A clear change from semiconducting to insulating behavior is observed at the charge localization temperature

TABLE 1
Unit Cell Parameters and Magnetic Data for $La_{0.5}Ca_{0.5}MnO_{3-\delta}$ ($0 \le \delta \le 0.5$) Samples

Composition	a	b	c	δ	Φ_K (K)	M_{Th}/f.u.	M_{Exp}/f.u.
$La_{0.50}Ca_{0.50}Mn^{4+}_{0.50}Mn^{3+}_{050}O_{3.00}$	5.407(2)	5.401(3)	7.629(2)	0.00	254.4	4.35 μ_B	5.02 $\mu_B \pm 0.2$
$La_{0.50}Ca_{0.50}Mn^{4+}_{0.50}Mn^{2+}_{0.50}O_{2.75}$	5.436(2)	5.421(1)	7.692(2)	0.25	102.0	4.86 μ_B	4.82 $\mu_B \pm 0.08$
$La_{0.50}Ca_{0.50}Mn^{4+}_{0.25}Mn^{2+}_{0.75}O_{2.50}$	5.361(3)	16.436(9)	5.340(3)	0.50	−155.0	5.39 μ_B	6.07 $\mu_B \pm 0.08$

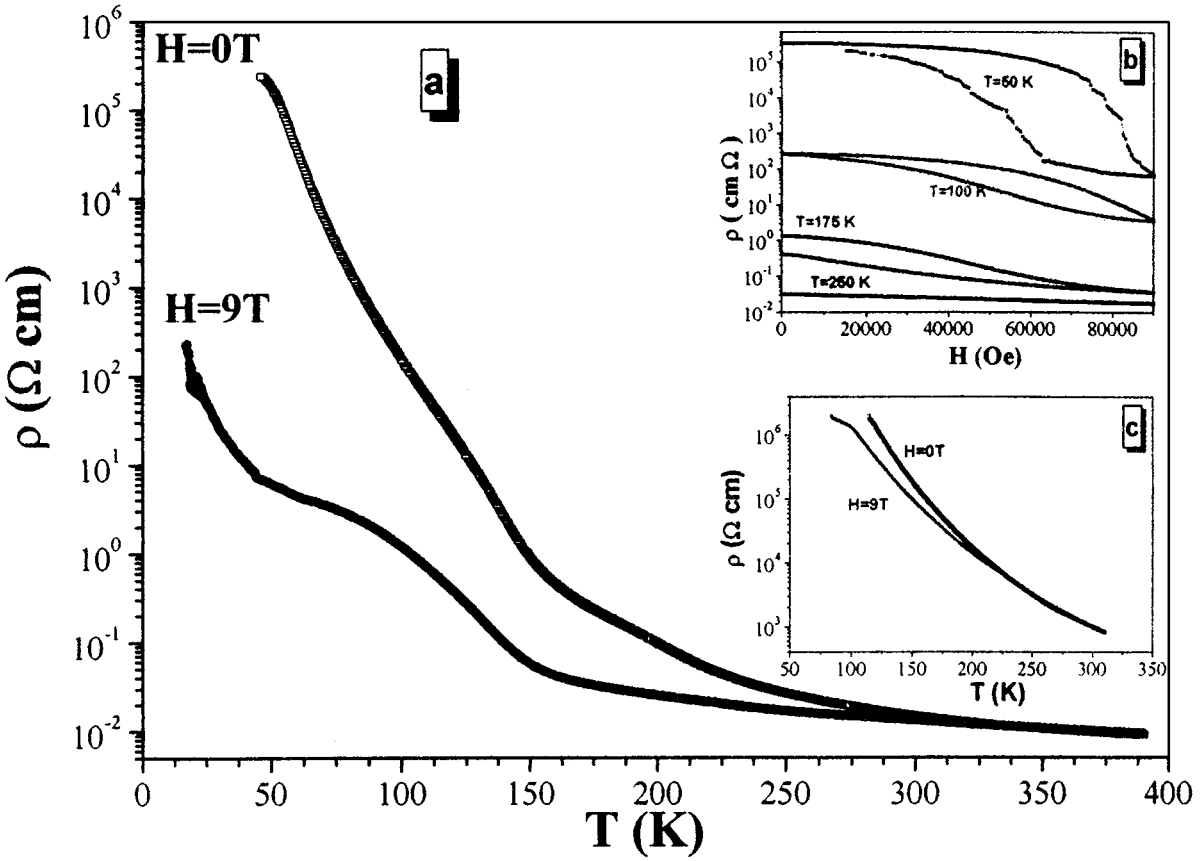

FIG. 8. (a) Temperature dependence of the resistivity for two magnetic fields (0 and 9 T) for the sample $La_{0.5}Ca_{0.5}MnO_{3.0}$. (b) Corresponding isotherm data. (c) Variation of resistivity showing the insulating behavior in the full temperature range for a sample with $\delta = 0.05$.

($T_{CO} \approx 190$ K), with a very strong hysteretic behavior on temperature. The isothermal data (Fig. 8b) shows a complicated behavior depending on the thermal and magnetic history. The temperature dependence of the magnetoresistance $(R_{H=0T} - R_{H=9T})/R_{H=0T}$ is shown in Fig. 9 and indicates a value close to 100% for $T < 125$ K, coincident with different authors (53). It is apparent that the origin of the drastic drop in resistivity on an applied magnetic field is related to the small amount of vacancies ($\delta = 0.05$ or higher), because the creation of anionic vacancies in $La_{0.50}Ca_{0.50}MnO_3$ produces a frustration of the magnetic ordering and the disappearance of the magnetoresistance and a clear insulating behavior in the full temperature range (Fig. 8c).

The paramagnetic moment calculated for the different compounds with $0 \leq \delta \leq 0.5$ shows a clear increase as δ increases, as is the case for the experimental value observed from magnetic susceptibility from $\delta = 0$ to 0.5. However, the experimental paramagnetic moments are almost 0.5 μ_B higher than the calculated moments. This difference between calculated and experimental paramagnetic moments is qualitatively higher if we do not consider the charge disproportion, so that the magnetic measurements will be in favor of higher amount of Mn^{2+}. Another possible explanation for the difference between the theoretical value (including Mn^{2+}) and the experimental, could be the formation of some kind of small superparamagnetic clusters, which later

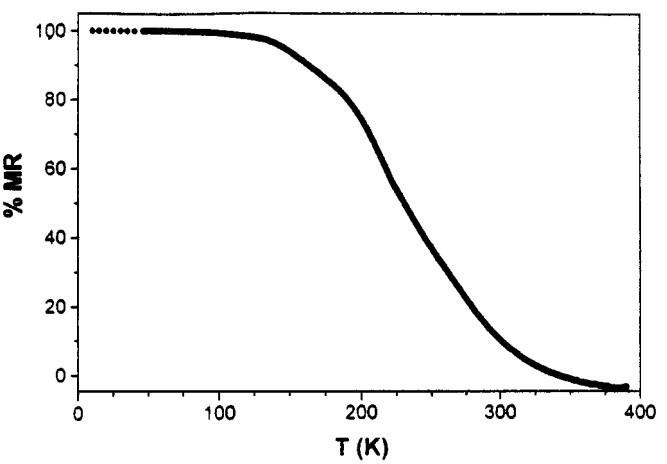

FIG. 9. Magnetoresistance measurements of $La_{0.5}Ca_{0.5}MnO_{3.00}$.

give rise to the irreversible behavior at low temperature and relieve the condition of a true paramagnetic moment. Only in the case of $\delta = 0.25$ are the experimental and calculated values inside the error. From $\delta = 0$ to 0.5, the main magnetic interation changes from mostly ferromagnetic ($\theta = 254$ K) to short range antiferromagnetic ($\theta = -155$ K). Also in the case of $\delta \approx 0$, the calculated paramagnetic moment is obtained in a limited temperature range $300 < T < 390$ K, which is reflected in a higher error. However, more experimental data as isothermal hysteresis loops are necessary in order to explain the complex magnetic behavior.

ACKNOWLEDGMENTS

We acknowledge the financial support of CICYT (Spain) through Research Projects MAT95-0642 and MAT98-0648.

REFERENCES

1. M. Verelst, N. Rangavittal, C. N. R. Rao, and A. Rousset, *J. Solid State Chem.* **104,** 74 (1993).
2. R. Mahendiran, R. Mahesh, A. K. Raychudhuri, and C. N. R. Rao, *J. Phys. D*: *Appl. Phys.* **28,** 1743 (1995).
3. R. Mahesh, R. Mahendiran, A. K. Raychudhuri, and C. N. R. Rao, *J. Solid State Chem.* **114,** 297 (1995).
4. R. Mahendiran, R. Mahesh, A. K. Raychudhuri, and C. N. R. Rao, *Solid State Commun.* **94,** 515 (1995).
5. R. Mahendiran, S. K. Tiwary, A. K. Raychudhuri, T. V. Ramakrishnan, R. Mahesh, N. Rangavittal, and C. N. R. Rao, *Phys. Rev. B* **53,** 3348 (1996).
6. R. Mahesh, R. Mahendiran, A. K. Raychudhuri, and C. N. R. Rao, *Appl. Phys. Lett.* **68,** 2291 (1996).
7. R. Mahesh, R. Mahendiran, A. K. Raychudhuri, and C. N. R. Rao, *J. Solid State Chem.* **122,** 448 (1996).
8. R. Mahendiran, S. K. Tiwary, A. K. Raychudhuri, R. Mahesh, and C. N. R. Rao, *Phys. Rev. B* **54,** 9604 (1996).
9. C. N. R. Rao, A. K. Cheetham, and R. Mahesh, *Chem. Mater.* **8,** 2421 (1996).
10. T. Vogt, A. K. Cheetham, R. Mahendiran, A. K. Raychudhuri, R. Mahesh, and C. N. R. Rao, *Phys. Rev. B* **54,** 15303 (1996).
11. N. Kumar and C. N. R. Rao, *J. Solid State Chem.* **129,** 363 (1997).
12. C. N. R. Rao and A. K. Cheetham, *Adv. Matter.* **9,** 1009 (1997).
13. A. Biswas, A. K. Raychudhuri, R. Mahendiran, A. Guha, R. Mahesh, and C. N. R. Rao, *J. Phys. Condens. Matter.* **9**, 355 (1997).
14. A. Arulraj, R. Gundakaram, A. Biswas, N. Gayathri, A. K. Raychudhuri, and C. N. R. Rao, *J. Phys. Condens. Matter.* **10,** 4447 (1998).
15. A. Arulraj, P. N. Santosh, R. S. Goplan, A. Guha, A. K. Raychudhuri, N. Kumar, and C. N. R. Rao, *J. Phys. Condens. Matter.* **10,** 8497 (1998).
16. C. N. R. Rao, P. N. Santosh, R. S. Singh, and A. Arulraj, *J. Solid State Chem.* **135,** 169 (1998).
17. P. V. Vaintha, R. S. Singh, S. Natarajan, and C. N. R. Rao, *J. Solid State Chem.* **137,** 365 (1998).
18. A. Arulraj, A. Biswas, A. K. Raychudhuri, C. N. R. Rao, P. M. Woodward, T. Vogt, D. E. Cox, and A. K. Cheetham, *Phys. Rev. B* **57,** 8115 (1998).
19. C. N. R. Rao, A. Arulraj, P. N. Santosh, and A. K. Cheetham, *Chem. Mater.* **10,** 2714 (1998).
20. R. von Helmolt, J. Wecker, B. Holzapfel, L. Schultz, and K. Samwer, *Phys. Rev. Lett.* **71,** 2331 (1993).
21. J. F. Lawler, J. G. Lunney, and J. M. D. Coey, *Appl. Phys. Lett.* **65,** 23 (1994).
22. S. Jin, T. H. Tiefel, M. McCormack, H. M. O'Bryan, L. H. Chen, R. Ramesh, and D. Schurig, *Appl. Phys. Lett.* **67**, 24 (1995).
23. C. Zener, *Phys. Rev.* **82,** 403 (1951).
24. P. Schiffer, A. P. Ramirez, W. Bao, and S. W. Cheong, *Phys. Rev. Lett.* **75,** 3336 (1995).
25. A. P. Ramirez, *J. Phys.*: *Condens. Mat.* **9,** 8171 (1997).
26. J. M. D. Coey, M. Viret, and L. Ranno, *Phys. Rev. Lett.* **75,** 3910 (1995).
27. Y. Tomioka, A. Asamitsu, H. Kuwahara, and Y. Tokura, *Phys. Rev. B* **53,** 1689 (1996).
28. H. Kuwahara, Y. Morimoto, Y. Tomioka, A. Asamitsu, M. Kasai, and Y. Tokura, *J. Appl. Phys.* **81,** 4954 (1997).
29. B. C. Tofield and W. R. Scott, *J. Solid State Chem.* **10,** 183 (1974).
30. J. H. Kuo, H. U. Anderson, an D. M. Sparlin, *J. Solid State Chem.* **83,** 52 (1989).
31. J. A. M. Van Roosmalen and E. H. P. Cordfunke, *J. Solid State Chem.* **110,** 106(1994).
32. J. A. M. Van Roosmalen, E. H. P. Cordfunke, R. B Helmholdt, and H. W. Zandbergen, *J. Solid State Chem.* **110,** 100 (1994).
33. J. A. Alonso, M. J. Martínez-Lope, M. T. Casais, J. L. MacManus-Driscoll, P. S. I. P. N. de Silva, L. F. Cohen, and M. T. Fernández-Díaz, *J. Mater. Chem.* **7,** 2139 (1997).
34. A. Reller, D. A. Jefferson, J. M. Thomas, R. A. Beyerlein, and K. R. Poeppelmeier, *J. Chem. Soc. Chem. Commun.* 1378 (1982).
35. K. R. Poeppelmeier, M. E. Leonowicz, J. C. Scanlon, J. M. Longo, and W. B. Yelon, *J. Solid State Chem.* **45,** 71 (1982).
36. A. Reller, J. M. Thomas, D. A. Jefferson, and M. K. Uppal, *Proc. R. Soc. London A* **394,** 223 (1984).
37. (a) G. H. Jonker and J. H. van Santen, *Physica* **16,** 377 (1950); (b) J. H. van Santen and G. H. Jonker, *Physica* **16**, 599 (1950).
38. A. Wold and R. J. Arnott, *J. Phys. Chem. Solids* **9,** 176 (1959).
39. M. Croft, D. Sills, M. Greenblatt, C. Lee, S. W. Cheong, K. V. Ramanujachary, and D. Tran, *Phys. Rev. B* **55,** 8726 (1997).
40. Y. H. Li, K. A. Thomas, P. S. I. P. N. de Silva, L. F. Cohen, A. Goyal, M. Rajeswari, N. D. Mathur, M. G. Blamire, J. E. Evetts, T. Venkatesan, and J. L. Macmanus-Driscoll, *J. Mater. Res.* **13,** 2161 (1989).
41. A. Urushibara, Y. Moritomo, T. Arima, A. Asamistu, G.Kido, and Y. Tokura. *Phys. Rev. B* **51**(20), 14–103 (1995).
42. P. G. Radaelli, M. Marezio, H. Y. Hwang, and S. W. Cheong, *J. Solid State Chem.* **122,** 444 (1996).
43. T. J. White, R. L. Segall, J. C. Barry, and J. L. Hutchison, *Acta Cryst. B* **41,** 93 (1995).
44. M. Vallet-Regi, J. M. González-Calbet, and M. A. Alario-Franco, J. C. Grenier, and P. Hagenmuller, *J. Solid State Chem.* **55,** 251 (1984).
45. A. Vegas, M. Vallet-Regí, J. M. González-Calbet, and M. A. Alario-Franco, *Acta. Cryst. B* **42,** 167 (1986).
46. A. M. Glazer, *Acta Cryst. B* **28,** 3384 (1972).
47. Von M. Harder and Hk. Müller-Buschbaum, *Z. Anorg. Allg. Chem.* **464,** 169 (1980).
48. J. M. González-Calbet, M. Vallet-Regí, M. A. Alario-Franco, and J. C. Grenier, *Mater. Res. Bull.* **18,** 285 (1983).
49. J. B. Wiley, M. Sabat, S. J. Hwu, K. R. Poeppelmeier, A. Reller, and T. Williams, *J. Solid State Chem.* **87,** 250 (1990).
50. R. D. Shannon, *Acta Crystallogr. A* **32,** 751 (1976).
51. J. A. M. Van Roosmalen and E. H. P. Cordfunke, *J. Solid State Chem.* **110,** 109 (1994).
52. J. A. M. Van Roosmalen and E. H. P. Cordfunke, *J. Solid State Chem.* **110,** 113 (1994).
53. G. Q. Gong, C. L. Canedy, G. Xiao, J. Z. Sun, A. Gupta, and W. J. Gallagher, *J. Appl. Phys.* **79,** 4538 (1996).